# Extracting Inner-Heliosphere Solar Wind Speed Information From Heliospheric Imager Observations

**L. A. Barnard[1]** , **M. J. Owens[1]** , **C. J. Scott[1]** , **and S. R. Jones[1]**

[1]Department of Meteorology, University of Reading, Reading, UK

**Abstract**  We present evidence that variability in the STEREO-A Heliospheric Imager (HI) data is correlated with in situ solar wind speed estimates from WIND, STEREO-A, and STEREO-B. For 2008–2012, we compute the variability in HI differenced images in a plane-of-sky shell between 20 to 22.5 solar radii and, for a range of position angles, compare daily means of HI variability and in situ solar wind speed estimates. We show that the HI variability data and in situ solar wind speeds have similar temporal autocorrelation functions. Carrington rotation periodicities are well documented for in situ solar wind speeds, but, to our knowledge, this is the first time they have been presented in statistics computed from HI images. In situ solar wind speeds from STEREO-A, STEREO-B, and WIND are all are correlated with the HI variability, with a lag that varies in a manner consistent with the longitudinal separation of the in situ monitor and the HI instrument. Unlike many approaches to processing HI observations, our method requires no manual feature tracking; it is automated, is quick to compute, and does not suffer the subjective biases associated with manual classifications. These results suggest we could possibly estimate solar wind speeds in the low heliosphere directly from HI observations. This motivates further investigation, as this could be a significant asset to the space weather forecasting community; it might provide an independent observational constraint on heliospheric solar wind forecasts, through, for example, data assimilation. Finally, these results are another argument for the potential utility of including a HI on an operational space weather mission.

**Plain Language Summary**  It would be useful for space weather forecasting to have a good estimate of the solar wind speed near the Sun. This could improve space weather forecasting models, and our knowledge of how the solar wind is formed and varies. However, estimating the solar wind speed near the Sun is difficult to do, with either with spacecraft that measure it directly or with cameras observing the solar atmosphere. We have analyzed variations in images of the solar wind taken by the Heliospheric Imagers on the STEREO-A spacecraft. We show that these variations are well correlated with solar wind speed measurements taken by in situ spacecraft. Furthermore, we show that these correlations evolve in a way that can be explained by the orbits of the spacecraft, which gives us increased confidence that that this statistical relationship is robust. Therefore, these results might be used to develop a relationship between variability in the Heliospheric Imager data and solar wind speed, which would allow us to estimate the solar wind speed near the Sun routinely. Such a technique would be useful for space weather forecasting and would be a good reason to put a Heliospheric Imager on any future space weather monitoring spacecraft.

## 1. Introduction

Effective space weather forecasting requires prediction of near-Earth solar wind conditions and hence modeling the solar wind environment of the inner heliosphere. For some time now it has been commonplace to use 3-D magnetohydrodynamic (MHD) models to represent the heliosphere (such as ENLIL, Odstrcil, 2003; MAS, Riley et al., 2001; and EUFORIA, Pomoell & Poedts, 2018). Such models are driven, indirectly, by photospheric and coronal observations, as their inner boundary conditions are typically derived from the output of coronal magnetic models and empirical parameterizations (e.g., the Wang-Sheeley-Arge extrapolation of potential field source surface solutions of the coronal magnetic field). Several recent studies demonstrate the success of this approach, with these models serving as useful research tools (Riley et al., 2012) and aiding skilful space weather forecasts (Riley et al., 2018).

However, as these models do not directly use any of the available heliospheric solar wind observations, an obvious question is "can solar wind observations be used to improve MHD modeling of the space weather environment?" The answer appears to be affirmative, as demonstrated by Lang et al. (2017), who showed that integrating a data-assimilation (DA) scheme into ENLIL improved ENLIL's representation of the inner heliosphere. Specifically, these authors performed a theoretical experiment that showed assimilating synthetic in situ plasma observations reduced the error of the model relative to the ground truth. Furthermore, Lang et al. (2017) and Lang and Owens (2019) highlight that it should be possible to improve heliospheric modeling by assimilating not only in situ plasma measurements but also remote sensing observations, such as those from Heliospheric Imaging instruments. Given the paucity of in situ monitors throughout the heliosphere, particularly out of the ecliptic plane, the possibility of assimilating remote sensing observations of the inner heliosphere is particularly interesting, as they may provide information over a much broader spatial domain than in situ monitors. We also note that, alongside visible-light instruments, radio observations are another complementary data source that might be used in an assimilative way, through techniques such as interplanetary scintillation.

The Heliospheric Imager (HI) instruments are wide-field visible-light imagers that have routinely observed the inner heliosphere since 2007, as part of the Sun-Earth-Connection-Coronal-Heliospheric-Investiation (SECCHI) instrument package aboard the twin STEREO spacecraft (STEREO-A and STEREO-B; Howard et al., 2008). The HI instruments primarily observe sunlight Thomson scattered off free electrons in the solar wind, and so, at the simplest level, these observations provide a measure of the solar wind electron number density along a line of sight (LOS) in the instrument's field of view (FOV). A key scientific focus for the HI observations has been characterizing the evolution and propagation of coronal mass ejections (CMEs) through the inner heliosphere (Harrison et al., 2017; Howard et al., 2008). Furthermore, in the context of space weather forecasting, these data led to the development of a plethora of techniques designed to predict the arrival of CMEs throughout the heliosphere (Harrison et al., 2017). However, much less research has been done into characterizing the background solar wind structure in the HI FOV, and what this may enable in a space weather forecasting context. That being said, the potential for extracting background solar wind information from HI observations has been demonstrated. Rouillard et al. (2008) showed that plasma parcels entrained into corotation interaction regions (CIRs) could be imaged in HI. Subsequently, Plotnikov et al. (2016) tracked many such events in HI images to study the long-term variability of CIRs and whether their arrival at Earth could be predicted from analysis of the HI images, demonstrating that they typically propagate at close to the slow solar wind speed ahead of the CIR, and their arrival near Earth can be predicted with an accuracy of several hours; these results broadly consolidate those from similar but independent studies by Davis et al. (2012) and Conlon et al. (2015). This line of research was further pursued by Sanchez-Diaz et al. (2017), who better quantified the temporal and spatial scales of plasma blobs released into the heliosphere near the heliospheric current sheet. They revealed that such blobs were released simultaneously across a wide range of longitudes, with a period of approximately 20 hr. However, although these studies have aided our understanding of the structure of the solar wind in the inner heliosphere, the analysis techniques they depend upon do not lend themselves to routine, global application, which is required to constrain MHD models of the solar wind with HI observations. This is because all of these studies required a large amount of manual classification in the HI observations, manually tracking features associated with CMEs, and plasma blobs acting as tracers for solar wind structures, using, for example, time-elongation plots (known colloquially as J-maps; Davies et al., 2009). Alongside this, we also note that DeForest et al. (2016) presented a groundbreaking analysis, which, through advanced processing of the HI images, revealed and quantified the onset of hydrodynamic turbulence in the young solar wind. This work analyzed 15 days of HI1 data from December 2008 in solar minimum and used structure function analysis to quantify how the texture of the images changed with radial distance.

There are also a range of image processing techniques that can be used to estimate the velocity of specific features within an image, or the the velocity throughout an entire image, which also do not require the manual tracking of features. For example, Pant et al. (2016) used the Hough transform to determine the kinematics of of CMEs in the HI1 FOV, based on earlier work by Robbrecht and Berghmans (2004), to develop the CACTus CME catalog from Coronagraph observations. Another branch of techniques falls under banner of optical flow estimation (Horn & Schunck, 1981). Optical flow techniques have been used successfully within solar physics to model CME kinematics in coronagraph images (Colaninno & Vourlidas, 2006), and chromospheric dynamics in Extreme Ultravoilet (EUV) imagers (Gissot & Hochedez, 2007; Gissot et al., 2008).

Additionally, DeForest et al. (2014) used Fourier transforms to extract information on the flow of Alfvén waves in coronagraph images of the outer corona. Our interest has focussed on describing the background solar wind flow with the HI instruments, and in doing so, we have experimented with different optical flow estimators. However, as of yet, we have been unsuccessful in robustly determining the background solar wind flow with these techniques and are unaware of any published works that successfully tackle this problem. From our own experiments, the reduced signal-to-noise ratio of HI images (relative to coronagraph and EUV images) was a key factor in limiting the success of this approach. Consequently, we have become interested in simpler and more empirical ways of constraining the background solar wind flow with heliospheric images.

Hence, within the context of our challenges to directly estimate the solar wind flow from HI images, here we explore the following question: Is there is a way to process the HI images that reveals aspects of the solar wind structure that might be sensibly used in conjunction with a DA scheme and MHD model of the solar wind? Ideally, such an algorithm would not require manual classification of the images and would rely on relatively simple metrics computed from the images, such that the analysis could be easily integrated into a solar wind modeling workflow. We posit that variability in HI differenced images can act as a tracer for solar wind structure and demonstrate that a measure of this variability has the same periodic structure as in situ solar wind plasma observations from different in situ monitors and can, in fact, be directly correlated with in situ solar wind plasma observations. Such an approach has promise, given the results of DeForest et al. (2016, 2018). In section 2 we introduce the in situ plasma observations and HI remote sensing data used throughout this investigation. Section 3 describes some statistical techniques used in our analysis, while the results are presented in section 4.

## 2. Data

Throughout this investigation we use white-light remote sensing observations of the inner heliosphere provided by the HI on STEREO-A, as well as in situ observations of the solar wind plasma provided by the WIND, STEREO-A, and STEREO-B spacecraft. Below we detail the provenance and processing of these data.

### 2.1. Heliospheric Imagers

The STEREO spacecraft, operational since late 2006, occupy approximately $1 AU$ heliocentric, ecliptic orbits, one ahead of (STEREO-A: STA) and the other behind (STEREO-B: STB) the Earth. Both STA and STB carry the SECCHI instrument package (Howard et al., 2008). Included in the SECCHI package is the HI instrument (Eyles et al., 2008), which consists of two wide-field white-light cameras (HI1 and HI2) that image solar wind structures propagating over a total elongation angle range from near 4° to around 90° from the Sun. During nominal science operations, the 20° FOV of HI1 is centered at 14° in the ecliptic plane, and the 70° FOV of HI2 is centered at 53.8°, also in the ecliptic plane. HI2 also includes a trapezoidal occulter, which was designed to limit the intense light from Earth at the start of the mission (Eyles et al., 2008), and restricts the outer edge of the central portion of the HI2 FOV to an elongation of around 74°. Throughout this work, we use only the observations provided by the HI1 camera on STA (HI1A), over the period spanning 1 January 2008 00:00 UT until 31 December 2012 23:59 UT. During this period, the nominal cadence of HI1 and HI2 science images is 40 and 120 min, respectively, while their binned pixel size is 70 arc-sec and 4 arc-min, respectively. More specifically, we use the level 2, 11-day background HI1A observations (made available at https://www.ukssdc.ac.uk/solar/stereo/data.html). The location of features in the HI1A FOV will be discussed in terms of Helioprojective-Radial-Coordinates: position angle ($\psi$), the anticlockwise angle from solar north, and elongation ($\epsilon$), the angular distance from Sun-center.

The photons detected by the HI instrument are primarily white-light solar photons, which have undergone Thomson scattering with free electrons in the solar wind. The signal received along any given LOS in the HI FOV is an integral along that line. But, as both the density of solar wind electrons and intensity of solar photons decreases with heliocentric radius, the signal received along a sight line is biased toward photons scattered on the surface of the sphere having a diameter defined by the Sun and observer as endpoints, originally termed the Thomson sphere (TS). However, we note that Howard and Deforest (2012) demonstrated that this bias was actually quite modest and also a broad function of distance along the LOS; hence, they argued it would be better referred to as the Thomson plateau.
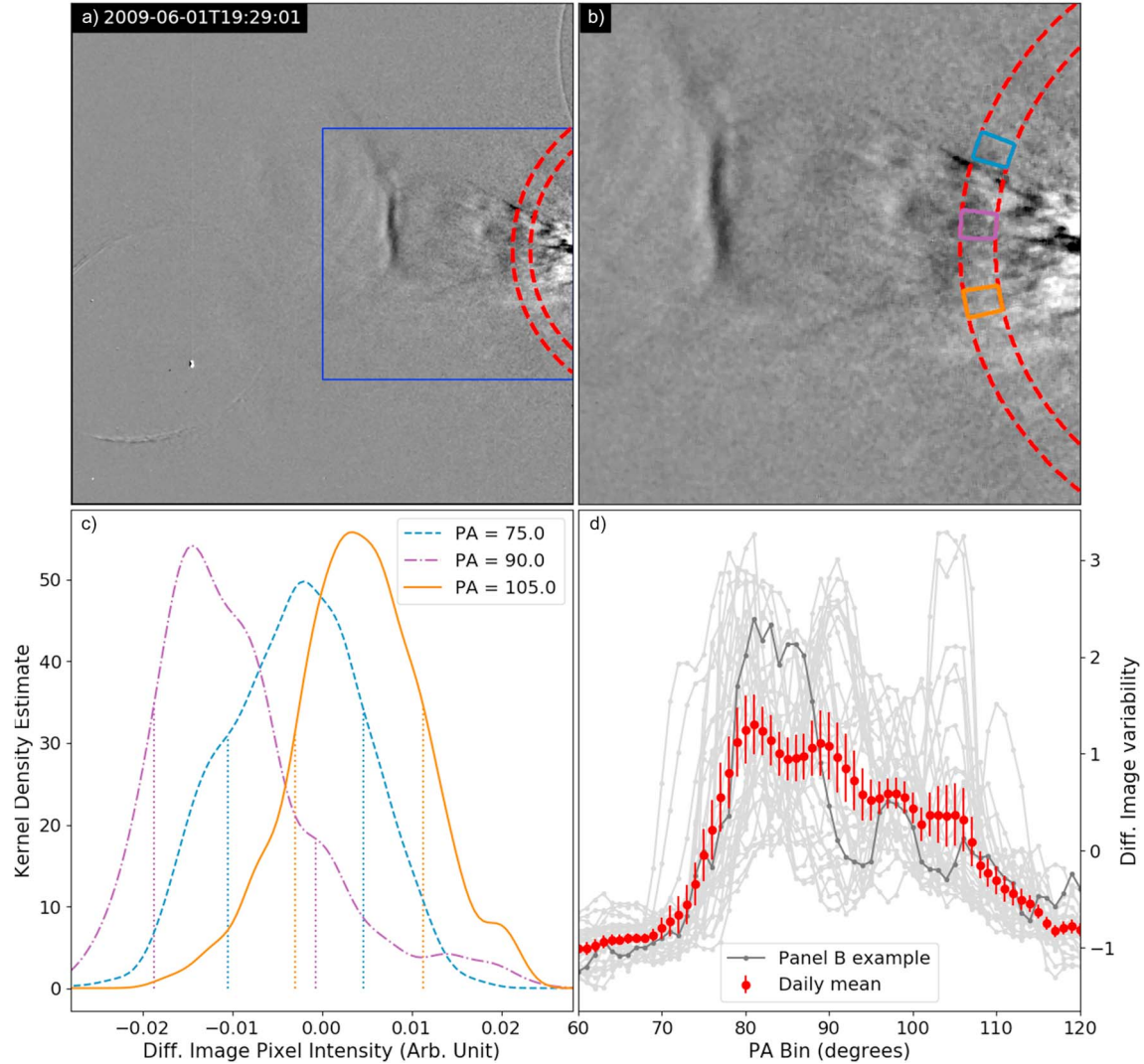
**Figure 1.** (a) An HI1A differenced image from 1 June 2009 1929 UT. The region enclosed in the blue square is the image segment shown in the expanded view in panel b, while the red-dashed contours show the elongations corresponding to plane-of-sky distances of 20–22.5 solar radii. (b) This expanded view of the HI1A differenced image shows more clearly the plane-of-sky region of interest, bounded by the red contours. Within this region, three position angle boxes are drawn at $\psi$ of 75°, 90°, and 105° by the blue, purple, and orange lines, respectively. (c) Kernel density estimates of the $I(\epsilon, \psi)$ values corresponding to the pixels within the three position angle boxes in panel b. Vertical dashed lines beneath each distribution show the $\pm\gamma(\psi)$ limits around the mean value, demonstrating that $\gamma(\psi)$ is a fair measure of the spread of these distributions. (d) The black line shows $\gamma_z(\psi)$ for the HI frame in panel b, while the gray lines show $\gamma_z(\psi)$ for the other Heliospheric Imager frames from 1 June 2009. The red points mark $\Gamma(\psi)$ for, while the uncertainty bars show one standard error of the mean.

### 2.1.1. HI Data Processing

Differenced images are produced from contiguous level 2, 11-day background subtracted HI1A images. The star fields are suppressed by identifying strong peaks in the image and replacing them with interpolated values from a 2-D cubic B-spline. Finally, a $5 \times 5$ median filter is applied to the differenced image. This is the same method as used in Barnard et al. (2017), and an example differenced image can be seen in Figure 1. The resulting image has a differenced image intensity field given by $I(\epsilon, \psi)$. We select a subsection of the image corresponding to the radial shell encompassing the plane-of-sky region spanning 20–22.5 solar radii, as shown by the red contours in Figures 1a and 1b. Within this shell, we measure the differenced image variability as a function of position angle by computing the standard deviation of $I(\epsilon, \psi)$ according to

$$\gamma(\psi) = \left( \frac{\left( \sum_{\psi-\delta\psi}^{\psi+\delta\psi} \sum_{\epsilon_{r1}}^{\epsilon_{r2}} I(\epsilon, \psi) - \left( \sum_{\psi-\delta\psi}^{\psi+\delta\psi} \sum_{\epsilon_{r1}}^{\epsilon_{r2}} I(\epsilon, \psi)/N \right) \right)^2}{N} \right)^{\frac{1}{2}}, \tag{1}$$

in position angle boxes 5° wide ($\delta\psi = 2.5°$), centered on every degree of $\psi$ from 60° to 120°, where $\epsilon_{r1}$ and $\epsilon_{r2}$ give the lower and upper elongation limits of the radial shell and $N$ is the number of pixels/samples in the position angle box. Examples of these boxes are shown for central position angles of 75°, 90°, and 105° by the blue, purple, and orange contours in Figure 1b.

In Figure 1c kernel density estimation is used to estimate the distribution of differenced image pixel brightness in the three position angle boxes marked in Figure 1b. Kernel density estimation is a nonparametric method used to estimate a parameters distribution function from a set of observations of that parameter. Each observation is assigned a prescribed distribution function (e.g., a Gaussian), and the normalized sum of these individual distributions is assumed to be a fair representation of a parameters true distribution function (Wilks, 1995). The vertical dotted lines beneath each distribution mark the region of $\pm\gamma$ about the mean brightness. Comparing the breadth of each $\pm\gamma$ region with the corresponding kernel density estimate, we conclude that the standard deviation is a reasonable measure of variability for these distributions. To facilitate comparison of $\gamma(\psi)$ across multiple frames, we then normalize $\gamma(\psi)$ in each frame, computing the $z$ score

$$\gamma_z(\psi) = \frac{\gamma(\psi) - \langle\gamma(\psi)\rangle}{\sigma_\gamma}, \tag{2}$$

where $\langle\gamma(\psi)\rangle$ and $\sigma_\gamma$ are the mean and standard deviation of $\gamma(\psi)$ within the radial shell in that frame. This is necessary, as the orbital motion of STEREO-A means the fixed radius plane-of-sky shell corresponds to elongation limits with a small annual variation. Furthermore, the intensity of HI images falls as approximately $\epsilon^{-3}$ (see DeForest et al., 2016), such that $\gamma(\psi)$ tends to lower values when the elongation limits are lager. Computing $\gamma_z(\psi)$ provides a normalized measure of the variability in each HI frame, allowing comparison throughout the HI time series.

This process is completed for every viable differenced image (differenced images cannot be computed if either or both frames are missing), returning a time series of differenced image variability as a function of position angle, $\gamma_z(\psi, t)$. We then compute the UT daily mean of this time series, $\Gamma(\psi, t)$, averaging the $\gamma_z(\psi, t)$ values at each position angle for each frame within a UT day. This process is demonstrated in Figure 1d; the black line shows $\gamma_z(\psi)$ for the differenced image presented in Figure 1a, while the gray lines show $\gamma_z(\psi)$ for all other frames obtained on 1 June 2009. The red circles show the daily mean value $\Gamma(\psi)$, with the uncertainty bars showing one standard error of the mean.

### 2.2. In Situ Solar Wind Plasma Observations
#### 2.2.1. WIND
The WIND spacecraft has, since 2004, continuously monitored properties of the in situ solar wind plasma while in a halo orbit of the Earth-Sun L1 Lagrange point. The Solar Wind Experiment instrument measures solar wind ion and electron properties, from which estimates of the solar wind bulk speed, density, and temperature have been computed (Ogilvie et al., 1995). Here, we use the 1-hr average solar wind bulk speed, density, and temperature estimates obtained from https://omniweb.gsfc.nasa.gov/.

#### 2.2.2. STEREO-A and STEREO-B
The STEREO spacecraft are also equipped with the Plasma and Supra-Thermal Ion Composition (PLASTIC) instrument payload, which measures in situ solar wind plasma properties (Kaiser et al., 2008). From these measurements, estimates of the solar wind bulk speed, density, and temperature have been derived, which we use in our following analysis. Similar to the WIND data, we use the 1-hr average solar wind bulk speed, density, and temperature estimates obtained from https://omniweb.gsfc.nasa.gov/, for both STA and STB.

### 2.3. Data Processing
From the 1-hr average time series, we compute daily means of the the solar wind speed, density, and temperature for WIND, STA, and STB, for every UT day in the period spanning 1 January 2008 to 31 December 2012. This results in 1,828 days of samples for each parameter, although we note that there were 2, 4, and 8 days where data availability meant valid daily means could not be computed for WIND, STB, and STA, respectively. Throughout the remainder of the article we refer to these quantities as $V_x$, $\rho_x$, and $T_x$, where the subscript $x$ takes the abbreviation of the spacecrafts name.

### 2.4. STEREO-A, STEREO-B, and WIND Orbits
Sections 2.1 and 2.2.1 described how STA and STB were in orbits drifting relative to Earth and that WIND was in a halo orbit around the L1 Lagrange point. Therefore, the relative locations of these three craft are
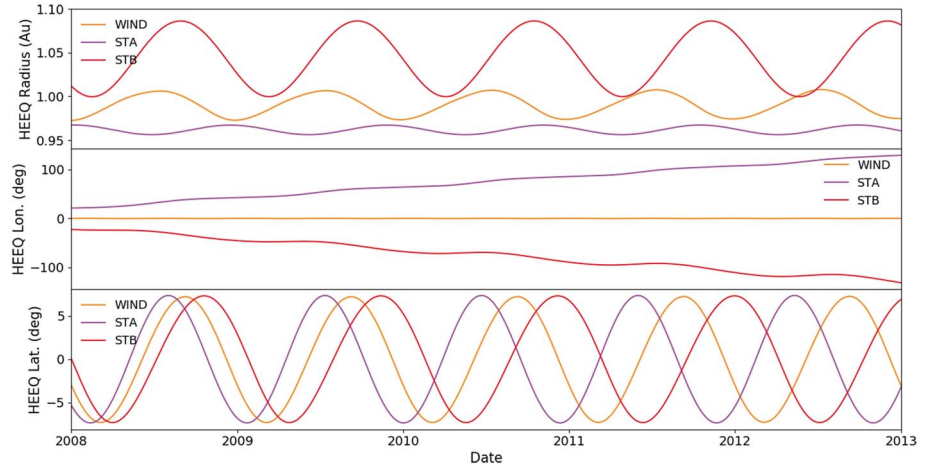
**Figure 2.** Time series of the Heliocentric Earth Equatorial coordinates of the WIND, STA, and STB spacecraft. The top, middle, and bottom spacecraft show the radial, longitudinal, and latitudinal coordinates, respectively.

continuously evolving, as described by Figure 2, which shows the Heliocentric Earth Equatorial (HEEQ) coordinates of WIND, STA, and STB, from 1 January 2008 until 31 December 2012. The top, middle, and bottom panels presents the HEEQ radius, longitude, and latitude, respectively. This shows that, for any time over this period, STA, STB, and WIND samples increasingly separate locations in the heliosphere. Consequently, when attempting to link these in situ solar wind observations with features in the HI remote sensing data, these three craft provide independent data that map to different elements in the full HI data set and so provide additional confidence that the statistical relationships we demonstrate below are robust.

## 3. Methods

### 3.1. Spearman's Rank Correlation

Spearmans's rank correlation is a correlation coefficient that provides a measure of the degree of association between two parameters (Wilks, 1995). This is a nonparametric statistical measure, as the degree of association is assessed on the ranks of the variables, rather than the actual values. Formally, for $N$ paired observations of two parameters $X$ and $Y$, Spearman's rank correlation coefficient $r_s$ is computed by first transforming the paired samples $X_i$ and $Y_i$ into their respective ranks $Rx_i$ and $Ry_i$ and then computing

$$r_s = \frac{\sum_i^N (Rx_i - \overline{Rx})(Ry_i - \overline{Ry})}{\sigma_{Rx}\sigma_{Ry}(N-1)}, \tag{3}$$

where $\overline{Rx}$ and $\sigma_{Rx}$, and $\overline{Ry}$ and $\sigma_{Ry}$, are the means and standard deviations of the ranks $Rx$ and $Ry$. Consequently, $r_s$ is a measure of how well the relationship between two variables may be modeled by a monotonic relationship. This differs from the more commonly used Pearson's product-moment correlation coefficient, which is a measure of how well two variables can be modeled with a linear relationship. Furthermore, interpretation of Pearson's correlation is complicated in situations when the paired samples do not form a bivariate normal distribution. The solar wind plasma properties and statistics computed from the HI images are not normally distributed, and there is no a priori reason to assume a linear relationship between them, hence using Spearman's rank correlation in this analysis.

Additionally, the statistical significance of $r_s$ can be computed, relative to a null hypothesis that there is no correlation between the samples (Wilks, 1995). Such a process cannot confirm that a relationship exists between the variables, but it can quantify how unusual it would be to obtain the sample correlation if the true correlation were zero. Here we employ a bootstrap resampling procedure to estimate the distribution of $r_s$ under the null hypothesis that the true correlation is zero. Under such a null hypothesis, the pairing of the samples is irrelevant, and so computing $r_s$ for many random realizations of the paired samples provides an empirical estimate of the distribution of $r_s$ under the null. By comparing the sample $r_s$ to the estimated null distribution, we can assess the likelihood of obtaining the sample $r_s$ due to random sampling of uncorrelated parameters.
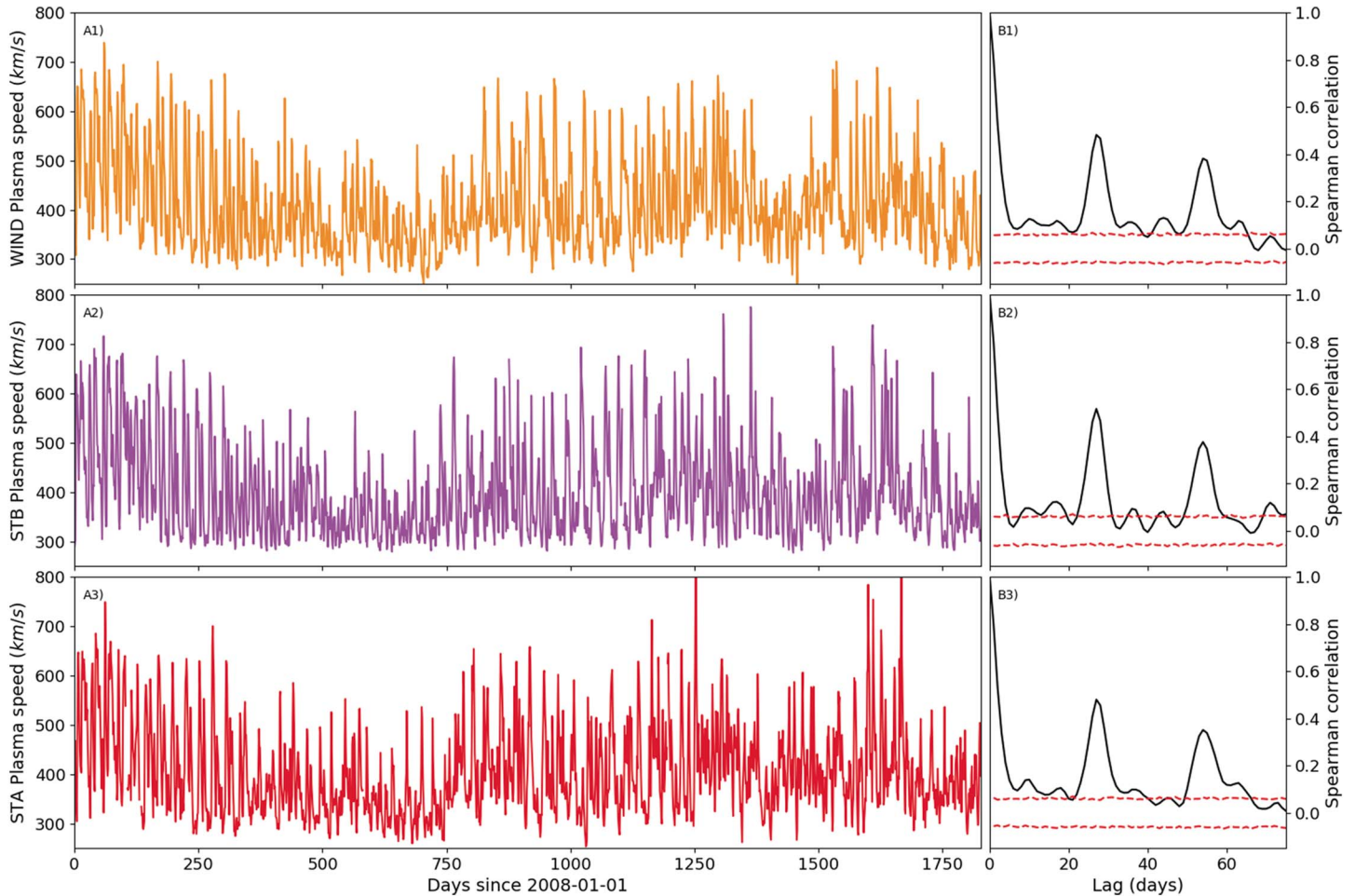
**Figure 3.** Panels A1:A3 show time series of daily mean solar wind speed estimates from WIND, STA, and STB, respectively, for the period of 1 January 2008 until 31 December 2012. Panels B1:B3 show the autocorrelation functions (solid black lines) of the daily mean solar wind speed values, for WIND, STA, and STB, respectively. The dashed red lines show the 0.5 and 99.5 percentiles of the estimated null distribution of $r_s$.

### 3.2. Autocorrelation Functions

Here we also compute the autocorrelation function (ACF) of solar wind plasma parameters and statistics derived from the HI images. An ACF is simply the correlation between a parameter and a lagged copy of itself, for a range of different lags. Any measure of correlation can be used to compute an ACF, and here we choose to compute the Spearman ACF.

Similar to computing the statistical significance of $r_s$ for a paired sample of two parameters, the significance of the ACF at any particular lag may also be estimated. This procedure is analogous to the case of a paired sample of two parameters, except that this must be applied at each lag.

## 4. Results

### 4.1. ACFs of $V$ and $\sigma_{hi}$

Figure 3 shows the time series and ACFs of $V$ for WIND, STA, and STB, respectively. These time series show the same broad features at WIND, STA, and STB, despite sampling increasingly different regions of the heliosphere throughout this period. For example, with increasing longitudinal separation, these monitors will experience different transient structures, and, even in a quiet and steady heliosphere, latitudinal differences mean the monitors still observe different solar wind structure. Panels B1:B3 present the ACFs of these $V$ data for WIND, STA, and STB (black lines). The red dashed lines show the 0.5 and 99.5 percentiles of the null distribution of $r_s$, estimated from the resampling procedure detailed in section 3.1. Each ACF has clearly defined maxima at lags of approximately 27 and 54 days, corresponding closely with the synodic solar rotation period/Carrington rotation time, as discussed by Owens et al. (2013).The ACF is computed
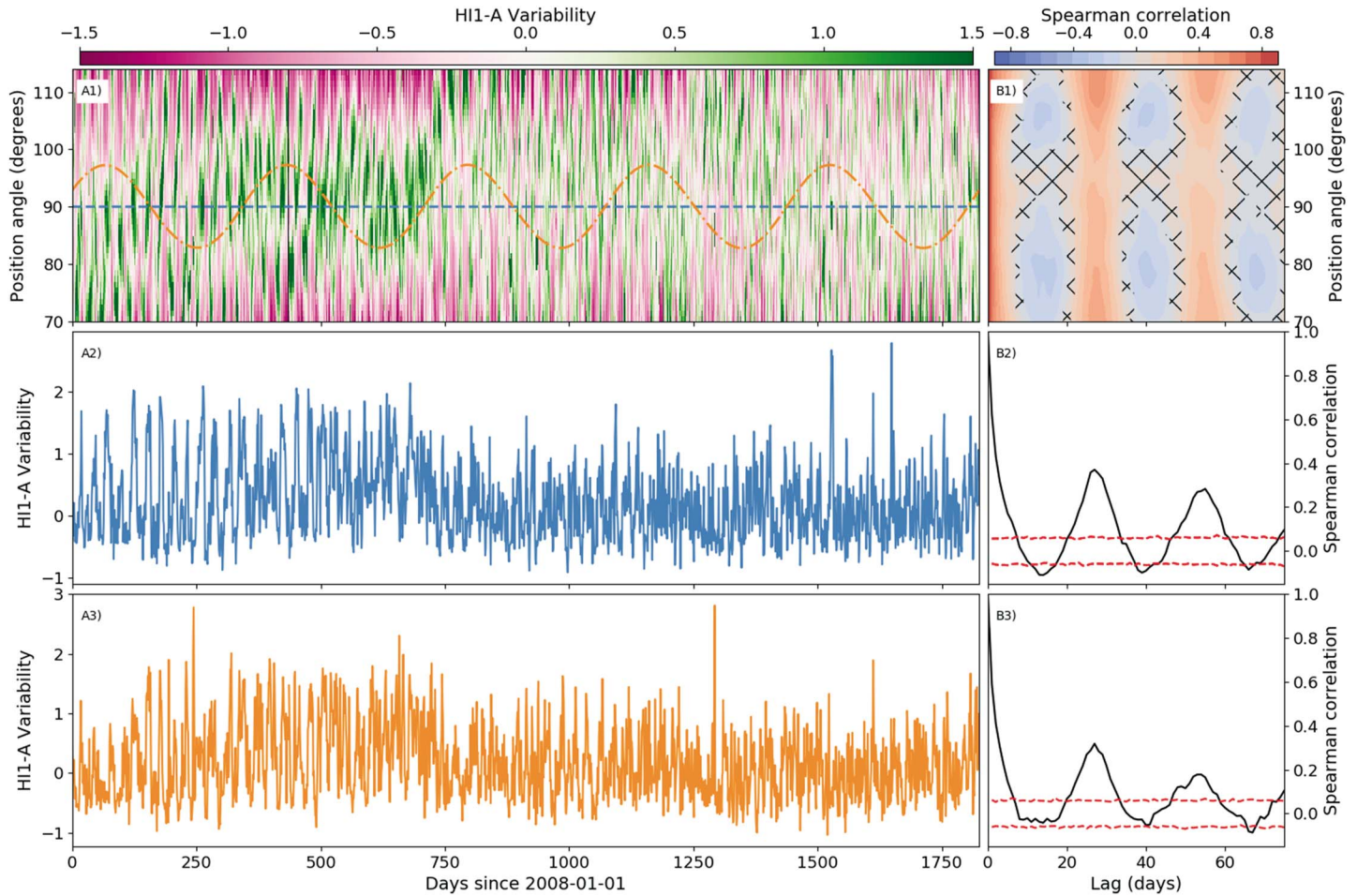
**Figure 4.** Panel A1: time series of the $\Gamma_{\psi,t}$ data, for all position angles considered. Pink and green regions show areas of lesser and greater $\Gamma_{\psi,t}$. Panels A2 and A3 present reduced versions of the $\Gamma_{\psi,t}$ data, corresponding to a $\psi$ slice of 90° and the $\psi$ variation of the WIND spacecraft, as marked by the blue dashed line and orange dash-dot line in panel A1, respectively. Panel B1: a contour plot of the autocorrelation functions computed along each $\psi$ of the $\Gamma_{\psi,t}$ data. Hatched regions highlight areas where the autocorrelation functions were within the 99% CI of the null distribution of $r_s$.

out to a lag of 75 days, and for much of this window the ACF values are larger than would be expected due to random sampling under the null hypothesis of zero correlation. We suggest that, between the maxima, the ACF is larger than expected for zero correlation possibly due to solar cycle scale variations introducing persistence at long timescales. Similar results are obtained for $\rho$ and $T$. For conciseness these figures are not included here but are available in the supporting information.

Figure 4 shows the time series of HI1A relative variability $\Gamma_{\psi,t}$, over the same time window as the $V$ data in Figure 3. Panel A1 shows the full series of $\Gamma_{\psi,t}$ for all computed position angles between 70° and 105°. Each vertical slice shows one daily mean, with green regions reflecting larger $\Gamma_{\psi,t}$, and pink regions smaller $\Gamma_{\psi,t}$. This shows that, broadly speaking, there is more variability near equatorial position angles (around 90°), and less variability at more polar position angles, similar to that shown in Figure 1d. There are more clearly defined boundaries between more and less variable regions earlier in the time series, which becomes more diffuse and complex after approximately day 750. Nonetheless, the time series in panel A1 is suggestive of periodic structure, which is investigated further in panel B1. The ACF of the $\Gamma_{\psi,t}$ data was computed for each $\psi$, and these data are presented as a contour of the ACF values as a function of $\psi$ and lag in panel B1. The significance of the ACF was computed using the same resampling procedure, and areas marked with diagonal hatching in the contour plot are within the 99% confidence interval of the null distribution of $r_s$. At all considered $\psi$, we observe the same approximately 27 and 54 day peaks in the ACF, similar to the ACFs of $V$, corresponding to the Carrington rotation time. Panels A2 and B2 present a reduced form of these data, showing only the time series of $\Gamma_{\psi,t}$ corresponding to the equatorial $\psi$ of 90°, as marked by the dashed blue
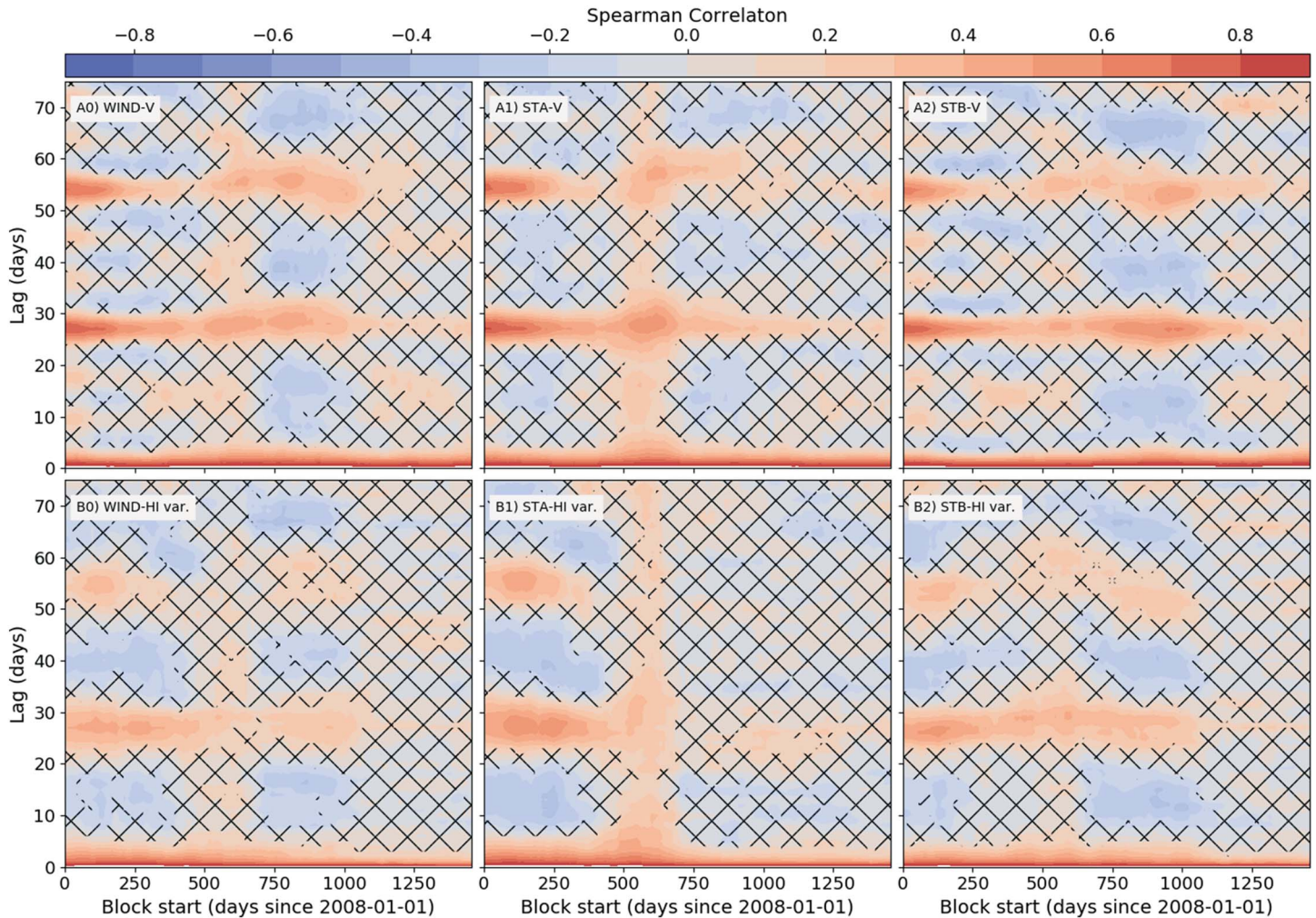
**Figure 5.** Each panel shows contours of the rolling window autocorrelation functions (ACFs) of the $V$ and $\Gamma_{\psi,t}$ data. Each ACF is computed for a 365 day window, stepped forward in 14 day blocks, and in each panel the $x$ axis shows the block start date, and the $y$ axis shows the ACF lag. Hatching shows regions where sample ACFs are inside the 99% CI of the null distribution of $r_s$. Panels A1:A3 show the rolling ACFs for $V_{wnd}$, $V_{stb}$, and $V_{stb}$, respectively, while panels B1:B3 show the rolling ACFs for $\Gamma_{\psi,t}$ along the $\psi$ traces of the WIND, STA, and STB spacecraft.

line in panel A1. Finally, panels A3 and B3 present the time series and ACF of $\Gamma_{\psi,t}$ data corresponding to the $\psi$ variation of the WIND spacecraft. This was computed by using nearest-neighbor interpolation to look up the $\Gamma_{\psi,t}$ values corresponding to the time-$\psi$ variation of WIND, as a synthetic example of how mapping a spacecraft orbit onto the $\Gamma_{\psi,t}$ data might differ from the ACFs observed for fixed $\psi$ considered in rows 1 and 2. In short, no significant change is observed between the ACFs corresponding to the fixed $\psi$ or $\psi$ variation matching WINDs orbit.

Although we are not certain what changes in HI variability, and its latitudinal structure, one possible explanation is the different nature of fast and slow solar wind, and the distribution of their source regions as a function of heliographic latitude. In situ observations show that the slow solar wind is typically more dense and more variable than fast solar wind, with differing turbulent profiles (Bruno & Carbone, 2013; Neugebauer & Snyder, 1966). We also note that Ko et al. (2018) recently argued that the magnitude of solar wind velocity fluctuations are a good discriminator between fast and slow solar wind, with slow solar wind typically showing smaller velocity fluctuations, although this work did not consider density fluctuations. Furthermore, in situ and remote observations demonstrate that fast solar wind originates from coronal holes, which tend toward more polar latitudes, particularly at solar cycle minimum (Schwenn, 2007; Zirker, 1977). Conversely, at solar cycle maximum, slow solar wind is not confined to equatorial regions and is emitted from a wider range of latitudes. Consequently, we might reasonably expect to observe more differenced image
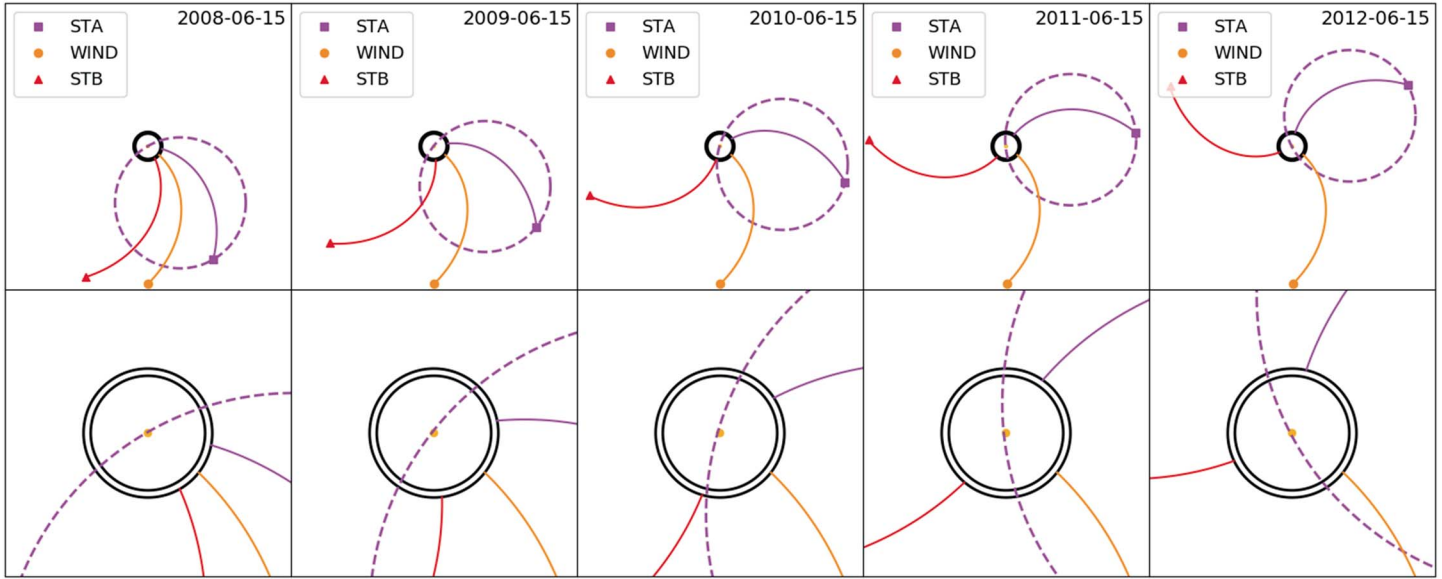
**Figure 6.** Schematic showing the relative locations of WIND, STA, and STB in the equatorial plane of Heliocentric Earth Equatorial coordinates, for the midpoint times of the calendar years analyzed here. Also shown are idealized Parker spiral streamlines connecting each spacecraft to the outer corona. Both rows show the locations of the spacecraft in the Sun's equatorial plane (Heliocentric Earth Equatorial $x$-$y$ plane), with the bottom row showing an enhanced view of the inner heliosphere. The purple dashed line shows the Thomson sphere of HI1A, while the black circles mark the equatorial intersection of the 20-22.5$R_s$ plane-of-sky shell used to compute $\Gamma(\psi, t)$.

variability along lines of sight containing more slow solar wind that is denser and more variable, and less differenced image variability alone lines of sight with more fast wind, which is less dense and less variable. Furthermore, this picture is consistent with the trend shown in Figure 4A1; There is a clearer distinction between variability at high and low latitudes from 2008 to 2010, during the low activity period spanning the solar cycle 23/24 transition, as the solar cycle progresses toward the maximum of solar cycle 24 (2014), there is less of a clear distinction between regions of high and low variability as a function of heliographic latitude. On the basis of this interpretation, we tentatively suggest there might be a negative correlation between HI variability and solar wind speed.

### 4.2. Rolling ACFs of $V$ and $\sigma_{hi}$

Of course, simply demonstrating that the ACFs of $V$ for different in situ monitors and also $\Gamma_{\psi,t}$ are remarkably similar over the period 1 January 2008 to 31 December 2012 is not, in isolation, good evidence that $\Gamma_{\psi,t}$ is a potentially useful tracer of solar wind structure. Another test is to examine how these ACFs evolve over the studied period. Here we do this by computing the ACFs in a rolling window for $V_{wnd}$, $V_{sta}$, and $V_{stb}$, and for traces extracted from $\Gamma_{\psi,t}$ that match the $\psi$ variations of WIND, STA, and STB. We use a rolling window 365 days wide, which is stepped forward in 14-day increments. These parameters were arbitrarily chosen, but the results are not sensitive to modest changes in the window width or step size (which was chosen to balance resolution with computational expense). The resulting ACF data are shown in Figure 5, which presents contours of the ACFs as a function of the block start date ($x$ axis) and lag ($y$ axis). Panels A0:A2 show the results for $V_{wnd}$, $V_{sta}$, and $V_{stb}$, while panels B0:B2 show the results for the $\psi$ traces extracted from $\Gamma_{\psi,t}$. Throughout, hatching marks areas where the ACF value falls inside the 99% CI limit for the null distribution of $r_s$.

For each monitor considered, there is clear similarity in the variability of the ACFs between $V$ and the $\Gamma_{\psi,t}$ slices. Considering the very different nature of the in situ solar wind speed estimates, and the HI differenced image variability data, we regard the similarity of these rolling ACFs as striking. Our tentative interpretation of this is that $\Gamma_{\psi,t}$ is serving as a metric for structure in the ambient solar wind, propagating though the TP of the HI1A FOV.

### 4.3. Correlation of $V$ and $\Gamma_{\psi,t}$

Given that there appears to be strong correspondence between the ACFs of the in situ solar wind speed estimates and $\Gamma_{\psi,t}$, we now consider directly the correlation between $\Gamma_{\psi,t}$ and $V$. However, if slices through
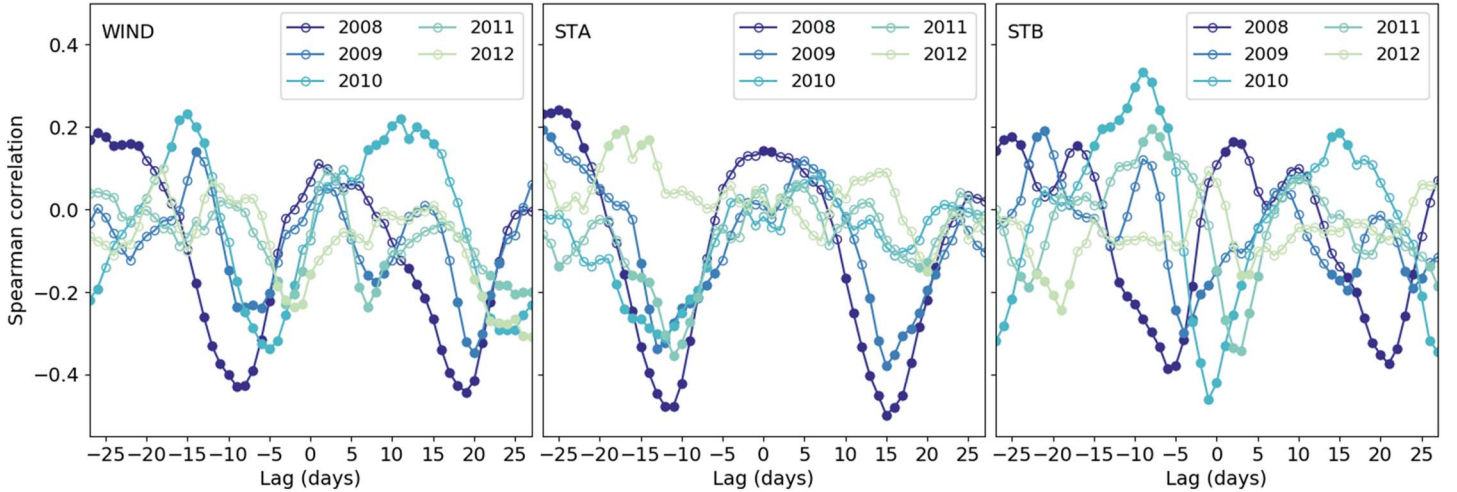
**Figure 7.** Lagged correlation between $\Gamma(\psi, t)$ and $V$ for WIND, STA, and STB. The time series were split into 1-year blocks, and the lagged correlation was computed within each year, for lags between $-27$ and $+27$ days. Successive years are plotted with lighter colors. Correlations outside of the 99% CI of the null distribution of $r_s$ are marked with a full marker, while those within the 99% CI of the null distribution are hollow.

$\Gamma_{\psi, t}$ are correlated with $V$, we should expect there to be some temporal lag between these measures, as at any given instant they observe properties of the solar wind that map to different source regions. Consequently, this lag is expected to be a function of the spatial separation of WIND, STA, and STB, recalling that these three pairs of craft have increasing longitudinal separation throughout the study period (Figure 2).

Figure 6 highlights this situation, presenting a schematic that shows the relative locations of WIND, STA, and STB, in the HEEQ equatorial plane, for the midpoint times of each calendar year considered here. The top row shows a view of the heliosphere out to the orbits of WIND, STA, and STB, giving the locations of these craft with orange, purple, and red markers. The black circles mark the 20–22.5 solar radii shell used in the HI image analysis, while the solid purple, orange, and red lines mark the idealized Parker spiral streamlines for radial wind of 400 km/s, serving as an approximate indicator of the foot point of the in situ monitors. The purple dashed line marks the location of the TS for HI1A. The bottom row shows an expanded view of the inner heliosphere, highlighting the relative locations of the intersections between the radial shell, approximate foot points of the in situ monitors, and TS of HI1A. From this, we form the following hypothesis; The lag between the observed $V$ and $\Gamma(\psi, t)$ values will vary in proportion to the separation between the approximate foot point longitude and the longitude of the intersection between the TS and radial shell. Consequently, the lag will be approximately constant for STA, due to colocation of HI1 and PLASTIC instruments on STA. Furthermore, as the foot points of STB and WIND drift closer to and past the TS intersection over 2008–2012, we expect that initially the lag will be closer to zero for STB than WIND, until eventually WIND is closer and has lags nearer zero. Finally, as STB and WIND drift at approximate 40° and 20° per year relative to STA, we expect the optimal lag for STB to change faster than the optimal lag for WIND.
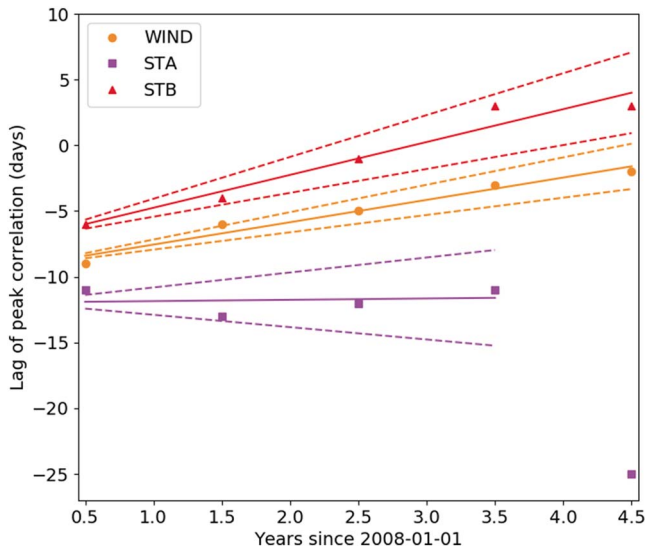


**Figure 8.** The lag of the minimum correlation between $\Gamma(\psi, t)$ and $V$ as a function of the midpoint time of the yearly blocks considered in Figure 7. The lag of minimum correlation steadily increases for STB and WIND, while is relatively constant for STA, excepting the outlier in the last year block. The solid lines show the standard least squares linear regression of each set of points, while the dashed lines give the $2\sigma$ errors on the gradient, the statistics of which are stated in Table 1. For STA, the outlying point in the last year block was not included in the regression.

To investigate this, we split the $V$ series into annual blocks for 2008–2012 (inclusive) and compute the lagged correlation between the $V$ series and the $\psi - t$ trace extracted from $\Gamma(\psi, t)$, for lags between $\pm 27$ days. Note that because of the annual variation in $\psi$ for each craft, the lag is applied to the lookup of the trace from $\Gamma(\psi, t)$; for $V(t, \psi)$, we look up $\Gamma(\psi, t + l)$, where $l$ is the lag. This simple approach is similar to one used in Riley and Lionello (2011), who used simple lagged correlations to relate modeled solar wind speeds at $30 R_s$ and at $1 AU$. Figure 7 presents these lagged

**Table 1**
*Gradients (and 2σ Errors) of the Regression Lines Shown in Figure 8*

|  | WIND | STA (no outlier) | STB |
|---|---|---|---|
| Gradient | $1.7 \pm 0.2$ | $0.1 \pm 0.5$ | $2.5 \pm 0.3$ |

correlations for each of WIND, STA, and STB, where each year is plotted in an increasingly light color. Filled circular markers highlight correlations, which fall outside of the 99% CI of the null distribution of $r_s$, assessed through resampling tests.

For each of WIND, STA, and STB, there are well-defined peaks in the lagged correlation. In particular, each craft displays two strong minima in the lagged correlation for most years, excepting only the 2012 period in STA and STB. In each year, these double minima are separated by approximately 27 days. We note this is consistent our interpretation of Figure 4, where we discussed that we might expect there to be a negative correlation between solar wind speed and HI variability.

The results of the lagged correlation are broadly consistent with our hypothesis, as described below. Consider first the lagged correlation of the STA data. The lags of the minima are relatively constant, indicative of the fixed relative locations of the HI1 and PLASTIC instruments on STA. We also note the approximately 3-day asymmetry between the two groups of the minima in STA (at approximately $-12$ and $+15$ days, respectively), which might be explained by the mean solar wind travel time between the source region and STA.

For both STB and WIND, the lags of the minima become more positive throughout 2008–2012. Considering the group of minima at more negative lags for each craft, they are initially closer to zero for STB and eventually become closer to zero for WIND. This is consistent with the expectations based on the drifting HEEQ longitudes of the approximate foot points of STB and WIND relative to the TS of STA and radial shell used to compute $\Gamma(\psi, t)$.

Figure 8 quantifies this relationship, plotting the lag of minimum correlation for each year, for WIND, STA, and STB. To compute this, we selected the group of minima at more negative lags for WIND and STB, and the group of minima between lags of $\pm 10$ days for STB. The markers show the lag of minimum correlation in years since 2008 (centered in the middle of the year block), while the solid lines show the linear regressions of these points, and the dashed lines the 2σ uncertainty on the gradient of the regression line. The gradients of these regression lines are given in Table 1. For STA, the outlying point in the last year block (Figure 8) was not included in the regression. These demonstrate that, as expected, for STA the drift in the lag of the minimum correlation is, within errors and excluding an outlier, consistent with zero. Furthermore, the drift in the minimum lag for STB is more rapid than for WIND, being approximately 1.5 times the WIND drift. Naively, we expected the STB drift to be approximately two times the WIND drift and do not currently understand why it is less than this, but within the uncertainties of this analysis we consider it broadly consistent with our earlier hypothesis.

## 5. Conclusions

We have demonstrated that, over the period 1 January 2008 to 31 December 2012, variability in differenced images from HI1A displays Carrington rotation periodicities, with an ACF remarkably similar to that obtained from in situ estimates of solar wind speed from WIND, STA, and STB. Furthermore, considering a sequence of shorter windows in this 5-year period, it was shown that the temporal evolution of the ACF was similar for the in situ solar wind speed estimates and HI differenced image variability.

It is perhaps not a great surprise that we have demonstrated Carrington rotation periodicities in HI1A differenced images. For example, it is well established that the HI instruments can be used to track the "Sheeley blobs" entrained into CIR structures (Rouillard et al., 2008), and subsequent work has revealed that these are observed to have a quasi-periodic release into the HI FOV, with a typical release timescale of approximately 19 hr, across a wide range of heliographic latitudes (Conlon et al., 2015; Sanchez-Diaz et al., 2016). CIR structures recur with approximately 27-day periods, and so it is plausible that measure of differenced image variability we use here, $\Gamma(\psi, t)$, is acting as a tracer for such structures. However, these prior works all relied on manual feature tracking in the HI FOV, to extract the $t$-$\epsilon$-$\psi$ variation of each blob. We are unaware of any work that has demonstrated Carrington rotation periodicities in simple statistics computed from the HI images.

Further to this, we have demonstrated a statistically significant correlation between HI1A differenced image variability and in situ estimates of solar wind speed from WIND, STA, and STB. Although it is always wise to be cautious of the results of a correlation analysis, we consider this a robust result as similar correlations were found for three independent in situ monitors that have sampled increasingly separate regions of the

heliosphere. Finally, there are systematic drifts in the correlation between in situ solar wind speed estimates and HI1A differenced image variability, which are well explained by the varying relative locations of the WIND, STA, and STB spacecraft.

If, as suggested here, a simple statistical analysis of HI1A images can provide an estimate of near-Sun solar wind speed structure, it increases the likelihood that heliospheric imaging can provide a valuable external constraint to MHD modeling of the heliospheric solar wind, through models such as ENLIL, MAS, and EUHFORIA. In particular, we are interested in investigating how HI data may be used within a DA scheme for heliospheric modeling, as per Lang et al. (2017) and Lang and Owens (2019). If it were found that HI observations could be used within a DA scheme for heliospheric modeling, it would provide a good argument for a HI to be included on any future operational space weather monitoring space craft.

Having said this, the analysis presented here is clearly exploratory, and it motivates a more thorough investigation of the relationship between heliospheric imaging and in situ solar wind parameters. In our opinion, there are several avenues of investigation that should be prioritized. First, we have used only the standard level 2 science data for HI1A. DeForest et al. (2011) presented a method for processing the HI observations, which increases the signal-to-noise ratio relative to standard level 2 data, referred to as L2S images by DeForest et al. (2016). These L2S images may better constrain the relationship between HI1 variability and in situ plasma observations. Furthermore, a particular limitation to our investigation is that we have not explored what scale-size features in HI might be best related to in situ observations. We employed a radial shell in the plane of the sky from 20–22.5$R_s$, position angle bins 5° wide and 1-day means, which means we are looking at only one scale of feature. An analysis that considers multiple scale sizes within the HI images would be informative in determining what features are best related to the in situ plasma observations.

# References

Barnard, L., de Koning, C. A., Scott, C. J., Owens, M. J., Wilkinson, J., & Davies, J. A. (2017). Testing the current paradigm for space weather prediction with heliospheric imagers. *Space Weather*, *15*, 782–803. https://doi.org/10.1002/2017SW001609

Bruno, R., & Carbone, V. (2013). The solar wind as a turbulence laboratory. *Living Reviews in Solar Physics*, *10*, 208. https://doi.org/10.12942/lrsp-2013-2

Colaninno, R. C., & Vourlidas, A. (2006). Analysis of the velocity field of CMEs using optical flow methods. *The Astrophysical Journal*, *652*, 1747–1754. https://doi.org/10.1086/507943

Conlon, T. M., Milan, S. E., Davies, J. A., & Williams, A. O. (2015). Corotating interaction regions as seen by the STEREO Heliospheric Imagers 2007-2010. *Solar Physics*, *290*(8), 2291–2309. https://doi.org/10.1007/s11207-015-0759-z

Davies, J. a., Harrison, R. a., Rouillard, a. P., Sheeley, N. R., Perry, C. H., Bewsher, D., et al. (2009). A synoptic view of solar transient evolution in the inner heliosphere using the Heliospheric Imagers on STEREO. *Geophysical Research Letters*, *36*, L02102. https://doi.org/10.1029/2008GL036182

Davis, C. J., Davies, J. a., Owens, M. J., & Lockwood, M. (2012). Predicting the arrival of high-speed solar wind streams at Earth using the STEREO Heliospheric Imagers. *Space Weather*, *10*, S02003. https://doi.org/10.1029/2011SW000737

DeForest, C. E., Howard, T. A., & McComas, D. J. (2014). Inbound waves in the solar corona: A direct indicator of Alfvén surface location. *The Astrophysical Journal*, *787*(2), 124. https://doi.org/10.1088/0004-637X/787/2/124

DeForest, C. E., Howard, T. A., & Tappin, S. J. (2011). Observations of detailed structure in the solar wind at 1 AU with STEREO/HI-2. *The Astrophysical Journal*, *738*(1), 103. https://doi.org/10.1088/0004-637X/738/1/103

DeForest, C. E., Howard, R. A., Velli, M., Viall, N., & Vourlidas, A. (2018). The highly structured outer solar corona. *The Astrophysical Journal*, *862*(1), 18. https://doi.org/10.3847/1538-4357/aac8e3

DeForest, C. E., Matthaeus, W. H., Viall, N. M., & Cranmer, S. R. (2016). Fading coronal structure and the onset of turbulence in the young solar wind. *The Astrophysical Journal*, *828*(2), 66. https://doi.org/10.3847/0004-637X/828/2/66

Eyles, C. J., Harrison, R. A., Davis, C. J., Waltham, N. R., Shaughnessy, B. M., Mapson-Menard, H., et al. (2008). The heliospheric imagers onboard the stereo mission. *Solar Physics*, *254*(2), 387–445. https://doi.org/10.1007/s11207-008-9299-0

Gissot, S. F., & Hochedez, J. (2007). Multiscale optical flow probing of dynamics in solar EUV images algorithm, calibration, and first results. *Astronomy and Astrophysics*, *1118*, 1107–1118. https://doi.org/10.1051/0004-6361:20065553

Gissot, S. F., Hochedez, J. F., Chainais, P., & Antoine, J. P. (2008). 3D reconstruction from SECCHI-EUVI images using an optical-flow algorithm: Method description and observation of an erupting filament. *Solar Physics*, *252*, 397–408. https://doi.org/10.1007/s11207-008-9270-0

Harrison, R. A., Davies, J. A., Biesecker, D., & Gibbs, M. (2017). The application of heliospheric imaging to space weather operations: Lessons learnt from published studies. *Space Weather*, *15*, 985–1003. https://doi.org/10.1002/2017SW001633

Horn, B. K. P., & Schunck, B. G. (1981). Determining optical flow. *Artificial Intelligence*, *17*(1-3), 185–203. https://doi.org/10.1016/0004-3702(81)90024-2

Howard, T. A., & Deforest, C. E. (2012). The Thomson surface. I. Reality and myth. *Astrophysical Journal*, *752*(2), 13. https://doi.org/10.1088/0004-637X/752/2/130

Howard, R. a., Moses, J. D., Vourlidas, A., Newmark, J. S., Socker, D. G., Plunkett, S. P., et al. (2008). Sun Earth connection coronal and heliospheric investigation (SECCHI). *Space Science Reviews*, *136*(1-4), 67–115. https://doi.org/10.1007/s11214-008-9341-4

Kaiser, M. L., Kucera, T. A., Davila, J. M., Cyr, O. C. St., Guhathakurta, M., & Christian, E. (2008). The STEREO Mission: An Introduction. *Space Science Reviews*, *136*(1-4), 5–16. https://doi.org/10.1007/s11214-007-9277-0

Ko, Y.-K., Roberts, D. A., & Lepri, S. T. (2018). Boundary of the slow solar wind. *The Astrophysical Journal*, *864*(2), 139. https://doi.org/10.3847/1538-4357/aad69e

Lang, M., Browne, P., van Leeuwen, P. J., & Owens, M. J. (2017). Data assimilation in the solar wind: Challenges and first results. *Space Weather*, *15*, 1490–1510. https://doi.org/10.1002/2017SW001681

Lang, M., & Owens, M. J. (2019). A variational approach to data assimilation in the solar wind. *Space Weather*, *17*, 59–83. https://doi.org/10.1029/2018SW001857

Neugebauer, M., & Snyder, C. W. (1966). Mariner 2 observations of the solar wind: 1. Average properties. *Journal of Geophysical Research*, *71*(19), 4469–4484. https://doi.org/10.1029/JZ071i019p04469

Odstrcil, D. (2003). Modeling 3-D solar wind structure. *Advances in Space Research*, *32*(4), 497–506. https://doi.org/10.1016/S0273-1177(03)00332-6

Ogilvie, K. W., Chornay, D. J., Fritzenreiter, R. J., Hunsaker, F., Keller, J., Lobell, J., et al. (1995). SWE, a comprehensive plasma instrument for the WIND spacecraft. *Space Science Reviews*, *71*(1-4), 55–77. https://doi.org/10.1007/BF00751326

Owens, M. J., Challen, R., Methven, J., Henley, E., & Jackson, D. R. (2013). A 27 day persistence model of near-Earth solar wind conditions: A long lead-time forecast and a benchmark for dynamical models. *Space Weather*, *11*, 225–236. https://doi.org/10.1002/swe.20040

Pant, V., Willems, S., Rodriguez, L., Mierla, M., Banerjee, D., & Davies, J. A. (2016). Automated detection of coronal mass ejections in stereo heliospheric imager data. *The Astrophysical Journal*, *833*(1), 1–15. https://doi.org/10.3847/1538-4357/833/1/80

Plotnikov, I., Rouillard, A. P., Davies, J. A., Bothmer, V., Eastwood, J. P., Gallagher, P., et al. (2016). Long-term tracking of corotating density structures using heliospheric imaging. *Solar Physics*, *291*, 1853–1875. https://doi.org/10.1007/s11207-016-0935-9

Pomoell, J., & Poedts, S. (2018). EUHFORIA: European heliospheric forecasting information asset. *Journal of Space Weather and Space Climate*, *8*(2014), A35. https://doi.org/10.1051/swsc/2018020

Riley, P., Linker, J. A., Americo Gonzalez Esparza, J., Jian, L. K., Russell, C. T., & Luhmann, J. G. (2012). Interpreting some properties of CIRs and their associated shocks during the last two solar minima using global MHD simulations. *Journal of Atmospheric and Solar-Terrestrial Physics*, *83*, 11–21. https://doi.org/10.1016/j.jastp.2012.01.019

Riley, P., Linker, J. A., & Mikić, Z. (2001). An empirically-driven global MHD model of the solar corona and inner heliosphere. *Journal of Geophysical Research*, *106*(A8), 15,889–15,901. https://doi.org/10.1029/2000JA000121

Riley, P., & Lionello, R. (2011). Mapping solar wind streams from the Sun to 1 AU: A comparison of techniques. *Solar Physics*, *270*, 575–592. https://doi.org/10.1007/s11207-011-9766-x

Riley, P., Mays, M. L., Andries, J., Amerstorfer, T., Biesecker, D., Delouille, V., et al. (2018). Forecasting the arrival time of coronal mass ejections: Analysis of the CCMC CME scoreboard. *Space Weather*, *16*, 1245–1260. https://doi.org/10.1029/2018SW001962

Robbrecht, E., & Berghmans, D. (2004). Automated recognition of coronal mass ejections (CMEs) in near-real-time data. *Astronomy and Astrophysics*, *425*(3), 1097–1106. https://doi.org/10.1051/0004-6361:20041302

Rouillard, A. P., Davies, J. A., Forsyth, R. J., Rees, A., Davis, C. J., Harrison, R. A., et al. (2008). First imaging of corotating interaction regions using the STEREO spacecraft. *Geophysical Research Letters*, *35*, L10110. https://doi.org/10.1029/2008GL033767

Sanchez-Diaz, E., Rouillard, A. P., Davies, J. A., Lavraud, B., Pinto, R. F., & Kilpua, E. (2017). The temporal and spatial scales of density structures released in the slow solar wind during solar activity maximum. *The Astrophysical Journal*, *851*(1), 32. https://doi.org/10.3847/1538-4357/aa98e2

Sanchez-Diaz, E., Rouillard, A. P., Lavraud, B., Segura, K., Tao, C., Pinto, R., et al. (2016). The very slow solar wind: Properties, origin and variability. *Journal of Geophysical Research: Space Physics*, *121*, 2830–2841. https://doi.org/10.1002/2016JA022433

Schwenn, R. (2007). Solar wind sources and their variations over the solar cycle. *Space Science Reviews*, *124*(1-4), 51–76. https://doi.org/10.1007/s11214-006-9099-5

Sunpy Community, T., Mumford, S. J., Christe, S., Pérez-Suárez, D., Ireland, J., Shih, A. Y., et al. (2015). SunPy Python for solar physics. *Computational Science & Discovery*, *8*(1), 14009. https://doi.org/10.1088/1749-4699/8/1/014009

Wilks, D. S. (1995). *Statistical methods in the atmospheric sciences* (pp. 467). London: Academic Press, London.

Zirker, J. B. (1977). Coronal holes and high-speed wind streams. *Reviews of Geophysics*, *15*(3), 257. https://doi.org/10.1029/RG015i003p00257